Sensors and Materials, Vol. 34, No. 12 (2022) 4705–4715
MYU Tokyo

S & M 3138

Rapid Subpixel Matching Method for Spaceborne Synthetic Aperture Radar Images

Zhong Wang, Chenglin Cai,* Mingjun Deng, Dongbo Zhang, and Zexian Li

School of Automation and Electronic Information, Xiangtan University, Xiangtan, Hunan 411105, China

(Received May 25, 2022; accepted October 19, 2022)

Keywords: SAR images, image matching, subpixel, block matching

With the development of synthetic aperture radar (SAR) technology, SAR images are being widely applied, such as in SAR image fusion and transformation detection, where image matching is a key procedure. In this paper, a practical and rapid subpixel matching method is proposed for spaceborne SAR images. The subpixel SAR-oriented features from an accelerated segment test (SAR-OFAST) detection operator is employed to improve the detection accuracy of keypoints. By determining the overlapping area of master–slave images, the search range of matching is reduced, and the strategy of block matching is adopted to save computing resources. To verify the accuracy and reliability of the proposed matching method, several groups of SAR images obtained with an identical observation orientation and diverse observation angles were tested using the proposed and other methods. Experimental results demonstrate that the proposed method has a higher speed than other methods with similar performance in other indicators, making it more suitable for scenarios requiring high efficiency.

1. Introduction

Synthetic aperture radar (SAR), an active microwave remote sensing imaging system, has been widely applied in many fields such as national defense, economy, agriculture, and environmental monitoring because of its advantages of all-day, all-weather, and high-resolution imaging.[1] With the increasing number of SAR satellites, more images are being acquired by SAR systems under diverse polarization modes, wavebands, and viewing angles. The use of these images in change detection, 3D reconstruction, super-resolution reconstruction, and other applications requires image matching.

Image matching is a method to automatically obtain homologous points between two images. A rapid and effective matching approach is required because of the large size of spaceborne SAR images and the long matching time. In addition, the detection accuracy of keypoints determines the effectiveness of feature-based matching methods.

Early research on image matching involved optical images. In this regard, many practical and effective algorithms have also been proposed for detecting features such as the Harris detection operator,[2] the features from an accelerated segment test (FAST) detection operator,[3] the scale-

*Corresponding author: e-mail: chengcailin@126.com
https://doi.org/10.18494/SAM3982

ISSN 0914-4935

invariant-feature transform (SIFT) algorithm,[4] and the speeded up robust features (SURF) algorithm,[5] an improved version of SIFT. By considering the efficiency of image matching, the oriented FAST and rotated BRIEF (ORB) algorithm[6] was proposed to greatly reduce the consumption time for image matching.

Speckle noise exists in SAR images because of the different imaging mechanisms used for SAR images and optical images and affects SAR image matching. For this reason, some scholars have improved keypoint detection by developing SAR-SIFT[7,8] and the bilateral filter SIFT (BFSIFT)[9] algorithm. Some scholars have also improved the extraction of descriptors by developing the multiscale Gabor odd filter (M-GOF)[10] and the radiation-variation insensitive feature transform (RIFT)[11] algorithm.[12–14] However, the construction of descriptors of these well-performing matching methods is often complicated, markedly increasing the matching time.

To address this problem, an improved ORB approach called SAR-ORB is proposed in this paper. By suppressing the speckle noise of SAR images, a procedure for keypoint extraction and descriptor construction using the ORB algorithm is proposed. A subpixel corner detection method to obtain subpixel keypoints is also introduced. To further improve the efficiency of SAR image matching, the geometric positioning information of SAR images is utilized to narrow the matching range of SAR images. In addition, the timeliness and accuracy of the matching results are improved by dividing the overlapping area of the master–slave images into small master–slave image pairs. The accuracy of the proposed method is evaluated using SAR image data with an identical observation orientation and diverse incidence angles and compared with experimental results obtained by SAR-SIFT, RIFT, and single-scale Gabor odd filter (S-GOF) algorithms. The experimental results indicate that the proposed method has an acceptable root mean square error (RMSE), high accuracy index, and high speed.

2. Proposed Method

Image matching mainly includes four processes: keypoint detection, feature description, keypoint matching, and mismatched point filtering. Because of the large size of SAR images, global matching consumes a large amount of computing resources, so the method of block matching is adopted in this work. The matching process is shown in Fig. 1.

2.1 Calculation of overlap region

Using the rational polynomial coefficients (RPCs) attached to spaceborne SAR images, the coordinates of four corners of one image in another image are calculated through forward and

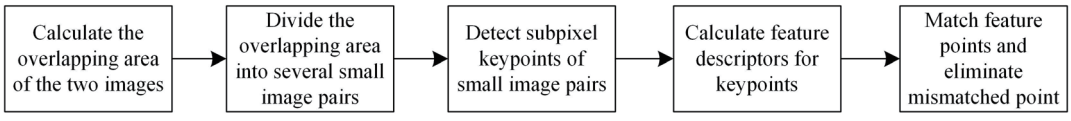

Fig. 1. Flowchart of the proposed method.

inverse transformation to obtain the overlapping area of the master–slave images. Figure 2 illustrates the conversion of the corner coordinates of an image into those of another image.

2.1.1 Calculation of ground coordinates

Through the RPC forward transformation, the ground coordinates corresponding to the corner coordinates of images can be obtained.[15] The formulas used are

$$\begin{cases} P = \dfrac{Num_P(X,Y,H)}{Den_P(X,Y,H)}, \\ L = \dfrac{Num_L(X,Y,H)}{Den_L(X,Y,H)}, \end{cases} \tag{1}$$

where (X, Y) represents the regularized image coordinates, (P, L, H) represents the regularized geographic coordinates [P is latitude, L is longitude, and H is the elevation at (P, L)], and, $Num_P(X, Y, H)$, $Den_P(X, Y, H)$, $Num_L(X, Y, H)$, and $Den_L(X, Y, H)$ represent the third-order polynomial terms of (X, Y, H).

Since the initial elevation H corresponding to corner O is unknown, Eq. (1) and the global 1-km-resolution digital elevation model (DEM) are used to iteratively find H, which is substituted into Eq. (1) to obtain the ground coordinates (P, L, H) corresponding to corner O.

2.1.2 Calculation of image coordinates

The image coordinates corresponding to the ground coordinates are obtained by the RPC inverse transformation.[16] The formulas used are

$$\begin{cases} X = \dfrac{Num_X(P,L,H)}{Den_X(P,L,H)}, \\ Y = \dfrac{Num_Y(P,L,H)}{Den_Y(P,L,H)}. \end{cases} \tag{2}$$

The corresponding image coordinates (X, Y) can be obtained by substituting the geographical coordinates (P, L, H) obtained in Sect. 2.1.1 into Eq. (2).

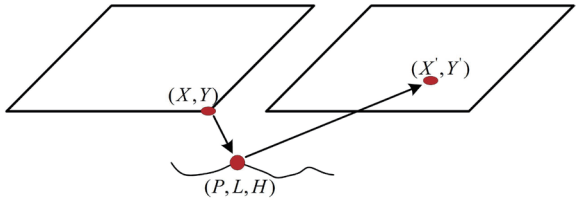

Fig. 2. (Color online) Illustration of image corner coordinate conversion.

2.1.3 Calculation of overlapping region

Through the method described in Sects. 2.1.1 and 2.1.2, the image coordinates of four corners of two corresponding SAR images can be calculated. By selecting the largest inscribed rectangular region within the range of the four points as the overlapping region of two master–slave SAR images, the search area is reduced. An example of overlapping areas is shown in Fig. 3, where the red box is the ultimately selected search area.

2.2 SAR image segmentation

The direct matching of two SAR images or their overlapping areas requires considerable computing resources. In this work, the search areas are divided into several non-overlapping small master–slave image pairs, which are matched in turn to obtain the final matching results. Specifically, the search area of the master image is divided into image blocks with a size of 600 × 600 (chosen after considering the effect of the number of block images and the reduced image size on computing resources), and the search area of the slave images is divided into the same number of small master–slave image pairs with the same length:width ratio between the search areas of the slave and master images. Finally, several small master–slave image pairs are obtained.

2.3 Subpixel SAR-OFAST

The oriented FAST (OFAST) process, a rapid corner detection process with an orientation component, is greatly affected by noise in the images when using the ORB algorithm,[6] while SAR images contain inherent speckle noise. Since corners are common on edges, they are usually detected in the edges. Some SAR image edge detection algorithms, such as the ratio of averages (ROA)[17] and ratio of exponentially weighted averages (ROEWA),[18] can effectively

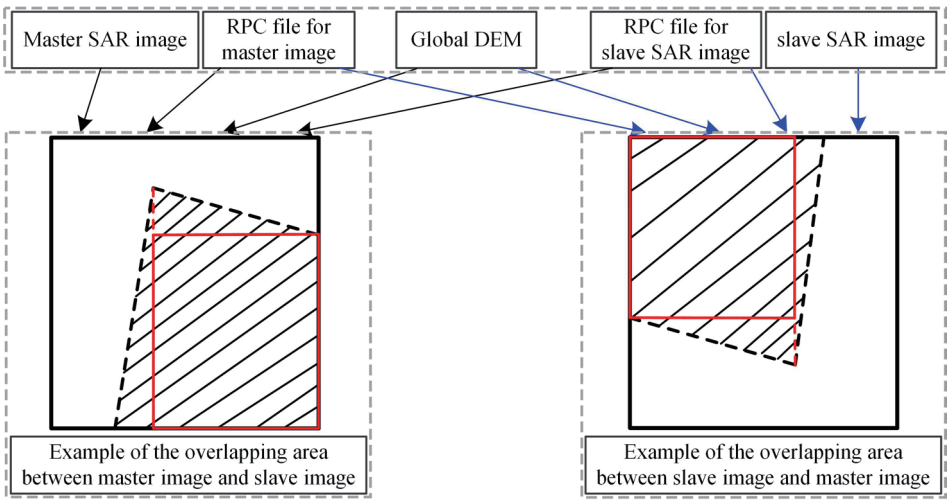

Fig. 3. (Color online) Overlapping area of two master–slave SAR images.

suppress speckle noise and detect SAR image edges. In this work, the ROEWA method is used to calculate the horizontal and vertical gradients of SAR images.

2.3.1 Calculation of SAR edge image

As an example, the mean of a pixel □($_0$, $_0$) in the direction $i = 3$ is defined as

$$\begin{cases} M_{1,\alpha}(i=3) = \int\limits_{x=R}\int\limits_{y=R^+} I(x_0+x, y_0+y)\cdot e^{-\frac{|x|+|y|}{\alpha}}, \\ M_{2,\alpha}(i=3) = \int\limits_{x=R}\int\limits_{y=R^-} I(x_0+x, y_0+y)\cdot e^{-\frac{|x|+|y|}{\alpha}}, \end{cases} \tag{3}$$

where α is the exponential weight.

The ratio gradient for orientation i is defined as

$$T_{i,\alpha} = \max\left(R_{i,\alpha}, \frac{1}{R_{i,\alpha}}\right) \text{ and } R_{i,\alpha} = \frac{M_{1,\alpha}(i)}{M_{2,\alpha}(i)}. \tag{4}$$

The ratio gradients in the horizontal ($i = 3$) and vertical ($i = 1$) directions can be calculated by Eq. (4). The SAR edge image can be acquired using

$$G_{n,\alpha} = \sqrt{T_{1,\alpha}^2 + T_{3,\alpha}^2}\ . \tag{5}$$

2.3.2 SAR-OFAST: FAST keypoint orientation

Since FAST does not generate multiscale keypoints, the scale edge pyramid of the SAR image, for which each edge layer is calculated as described in Sect. 2.3.1, is employed, and the FAST keypoints are detected at each edge layer of the pyramid. The number of initial features selected from each layer decreases with decreasing scale factor per edge gradient layer. The intensity centroid is used to compute the orientation of corners obtained by FAST.

2.3.3 Calculation of subpixel corner

Since most corner coordinates are not integers, more accurate corner coordinates (i.e., subpixel corner coordinates) must be calculated. Therefore, a subpixel corner detection method is introduced to calculate the keypoints obtained in Sect. 2.3.2; thereby, the coordinates of subpixel features are obtained. Details of the method are described as follows.

There are two cases for a point near a corner: one is an edge point, which is perpendicular to the gradient direction of the edge point, such as point p_1 in Fig. 4; the other is a point located in a smooth area, whose gradient is 0, such as point p_0 in Fig. 4. Thus, we can define

$$G_i * (p_i - q) = 0 , \tag{6}$$

where q represents a subpixel corner, p_i represents a point in the neighborhood of the corner, and G_i is the gradient at point p_i.

Because different points in a neighborhood have different influences on the corner, the Gaussian weight is introduced into Eq. (6); thus, the coordinate of corner q is

$$q = \sum_{i=1}^{N} (G_i^{\mathrm{T}} G_i \omega_i)^{-1} (G_i^{\mathrm{T}} G_i \omega_i p_i) , \tag{7}$$

where ω_i is the Gaussian weight at point p_i and N is the number of points in the corner's neighborhood.

A 7 × 7 neighborhood centered on corners detected by the SAR-OFAST operator is selected to solve the subpixel corners iteratively.

2.4 SAR image matching

Using the keypoints calculated in Sect. 2.3, the BRIEF approach[6] is applied to construct local binary descriptors of the neighborhoods of keypoints. The Hamming distance between descriptors is taken as the metric criterion, and a brute force algorithm is adopted to roughly match the selected keypoints. The grid-based motion statistics (GMS)[19] mismatch elimination algorithm is used for coarse matches, and the matching result of each small master–slave image pair is finally obtained.

All small segmented master–slave image pairs are matched, and the obtained matching results are combined. In the global scope of the overlapping region, the fast sample consensus (FSC) algorithm[20] is applied to remove the mismatches, and the ultimate matches of the two SAR images are obtained.

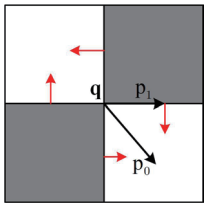

Fig. 4. (Color online) Example graph of subpixel corner neighborhood gradient.

3. Experimental Results

To verify the performance of the proposed method, we conducted experiments on several groups of master–slave SAR images of identical resolution with identical observation orientation and diverse observation angles. Details of the experimental data are given in Table 1. The obtained results were compared with the matching results for SAR-SIFT, RIFT, and S-GOF algorithms (reproduced by C++ in accordance with relevant papers). All experiments were performed on a desktop PC with an Intel Core i9 3.5 GHz processor and 128 GB RAM.

3.1 Assessment metrics

(1) Number of correct matches (NCM): For every master–slave SAR image pair, 100 pairs of homologous points are manually marked. Then the affine transformation model between SAR images is estimated by the marked homologous points. Finally, a distance threshold of 1.5 pixels is used to further filter the matches filtered by the GMS algorithm. The match satisfying the norm (the distance threshold of 1.5 pixels) is correct.
(2) Precision: Precision is defined as NCM/NM, where NM is the number of matches filtered by the GMS algorithm.
(3) RMSE: The RMSE is defined as

$$RMSE = \sqrt{\frac{1}{NCM}\sum_{i=1}^{NCM}\left(\left(x_i - x_i'\right)^2 + \left(y_i - y_i'\right)^2\right)}, \tag{8}$$

where (x_i, y_i) is the correct keypoint of the master SAR image and (x'_i, y'_i) is the corresponding homologous point after the affine transformation.
(4) Average computational time (ACT): This is the average computational time required to match each small master–slave image pair. If there is only one small master–slave image pair, the computational time is considered as ACT.

Table 1
Experimental data.

Image	Orbit	Side direction	Angle of incidence	Image size	Resolution (m)
Im1	Ascending	Right	48.02	10024 × 11458	3
Im2	Ascending	Right	48.83	10024 × 11432	3
Im3	Ascending	Right	45.54	10024 × 11419	3
Im4	Ascending	Right	53.79	11048 × 10068	3
Im5	Descending	Right	54.55	11048 × 10373	3
Im6	Descending	Right	50.90	10706 × 11021	3
Im7	Descending	Right	46.10	10024 × 11754	3
Im8	Ascending	Left	50.34	10706 × 10972	3
Im9	Ascending	Left	46.99	10024 × 11730	3

3.2 Experimental analysis

Firstly, selecting the small master–slave SAR image pair of Im1 and Im2, we compare our matching results with those of the SAR-SIFT, RIFT, BFSIFT, S-GOF, and M-GOF algorithms. The matching results are shown in Fig. 5, which shows similar distributions on homologous points. Figure 5(f) shows that the proposed method has similar performance to that of the other methods in the abundantly textured built-up area but poor performance in the afforested and other areas. As can be seen from Table 2, the proposed approach has the highest performance in terms of efficiency (i.e., the minimum computational time), although other metrics have slightly

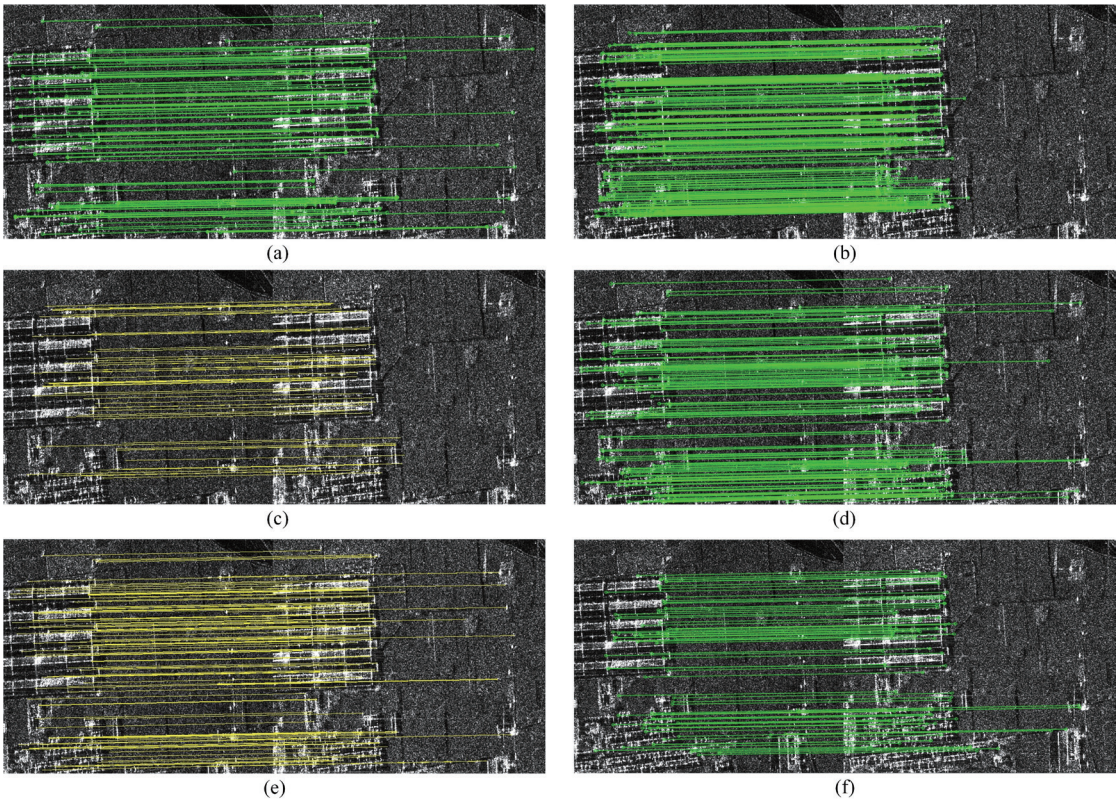

Fig. 5. (Color online) Matching result of the small master–slave image pair of Im1 and Im2: (a) SAR-SIFT algorithm, (b) RIFT algorithm, (c) BFSIFT algorithm, (d) S-GOF algorithm, (e) M-GOF algorithm, and (f) proposed algorithm.

Table 2
Contrast matching results of a small master–slave SAR image pair.

Image pair	Method	NCM	RMSE	Computational time (s)
Im1 & Im2	SAR–SIFT	82	0.893	1.726
	RIFT	90	0.841	17.137
	BFSIFT	69	0.872	3.025
	S-GOF	95	0.710	20.513
	M-GOF	**102**	**0.695**	23.728
	Proposed	78	0.801	**0.529**

lower performance. Therefore, in the case of good performance of other indicators, the proposed method is more efficient than the other algorithms.

Ten matching tests were conducted using the proposed method and the other matching algorithms. Table 3 shows the results obtained.

Table 3
Results obtained with diverse matching methods.

Image pair	Method	Blocks	NM	NCM	Precision	RMSE	ACT (s)
Im1 & Im2	SAR-SIFT	195	29383	7646	0.260	1.016	1.689
	RIFT		51476	11332	0.220	0.782	16.756
	BFSIFT		25658	7348	0.286	0.947	3.103
	S-GOF		47233	11147	0.236	0.703	21.237
	M-GOF		54357	12564	0.231	0.714	24.035
	Proposed		23513	7245	0.308	0.848	0.541
Im1 & Im3	SAR-SIFT	285	18632	4392	0.236	0.984	1.701
	RIFT		14893	3986	0.268	0.823	16.433
	BFSIFT		13765	4035	0.293	0.967	3.043
	S-GOF		16260	4504	0.277	0.724	20.401
	M-GOF		17943	4701	0.262	0.734	24.147
	Proposed		12325	3834	0.311	0.829	0.515
Im1 & Im4	SAR-SIFT	288	4021	676	0.168	0.963	2.316
	RIFT		4868	857	0.176	0.802	17.768
	BFSIFT		3564	624	0.176	0.945	3.062
	S-GOF		4209	926	0.220	0.764	22.329
	M-GOF		4927	1034	0.210	0.743	24.357
	Proposed		2298	602	0.262	0.849	0.457
Im2 & Im3	SAR-SIFT	168	9157	2320	0.253	0.986	2.436
	RIFT		10635	2669	0.251	0.785	19.719
	BFSIFT		8427	2347	0.279	0.941	3.049
	S-GOF		14834	3817	0.257	0.717	22.780
	M-GOF		15124	4018	0.266	0.728	24.146
	Proposed		6785	1896	0.279	0.821	0.583
Im2 & Im4	SAR-SIFT	238	4710	1155	0.245	0.934	2.261
	RIFT		5242	1236	0.236	0.802	18.937
	BFSIFT		3516	917	0.261	0.951	3.082
	S-GOF		7238	2106	0.291	0.756	22.038
	M-GOF		7936	2284	0.288	0.762	24.316
	Proposed		2919	806	0.276	0.756	0.549
Im3 & Im4	SAR-SIFT	238	4658	846	0.182	0.947	2.232
	RIFT		3894	745	0.191	0.834	19.218
	BFSIFT		3726	718	0.193	0.956	3.061
	S-GOF		5362	1169	0.218	0.797	21.686
	M-GOF		5719	1354	0.237	0.763	24.126
	Proposed		2259	512	0.227	0.830	0.547
Im5 & Im6	SAR-SIFT	272	9936	2515	0.253	0.955	2.187
	RIFT		15464	3929	0.254	0.794	17.651
	BFSIFT		8747	2614	0.299	0.976	3.057
	S-GOF		17178	4064	0.237	0.732	21.844
	M-GOF		18246	4658	0.255	0.736	24.039
	Proposed		7967	2397	0.301	0.805	0.509

Table 3
(Continued).

Image Pair	Method	Blocks	NM	NCM	Precision	RMSE	ACT (s)
Im5 & Im7	SAR-SIFT	288	3003	726	0.242	0.966	2.411
	RIFT		4297	1134	0.264	0.795	22.512
	BFSIFT		2865	702	0.245	0.982	3.095
	S-GOF		6705	1978	0.295	0.740	23.201
	M-GOF		7012	2048	0.292	0.713	24.237
	Proposed		2625	671	0.256	0.790	0.573
Im6 & Im7	SAR-SIFT	252	22884	5264	0.230	0.976	2.407
	RIFT		40189	9967	0.248	0.789	22.498
	BFSIFT		20972	4856	0.232	0.936	3.116
	S-GOF		33325	10264	0.308	0.720	22.836
	M-GOF		38156	10089	0.264	0.735	24.327
	Proposed		23513	7245	0.308	0.848	0.541
Im8 & Im9	SAR-SIFT	234	7218	1725	0.239	0.961	2.136
	RIFT		11351	2202	0.194	0.828	21.132
	BFSIFT		6436	1535	0.239	0.975	3.048
	S-GOF		11349	2902	0.258	0.730	22.185
	M-GOF		12647	3146	0.249	0.714	24.175
	Proposed		6137	1754	0.286	0.823	0.489

As can be seen from Table 3, although NM and NCM of the proposed method are usually the lowest for the ten matching pairs, the minimum NCM of the proposed method can exceed 500, which can meet the minimum quantity requirements of subsequent applications. In addition, in all the experiments, the proposed method is the fastest, usually requiring about 0.5 s. The RMSE of the ten experiments is less than 1 pixel, substantially superior to those for RIFT, SAR-SIFT, and BFSIFT and slightly inferior to those for S-GOF and M-GOF. Moreover, the precision of the proposed method is substantially the highest.

The results indicate that the proposed method is generally superior to the other algorithms in terms of indicators, although the NCM has a low value. In general, with increasing difference in the incidence angle between the master and slave images, the geometric distortion between surface features becomes larger, resulting in a lower NCM. Moreover, homologous points are evenly distributed in overlapping areas but less evenly distributed in afforested and mountainous areas. Note that not all the tests employ parallel computing or GPU acceleration, which would further increase the running speed.

4. Conclusions

In this work, a real-time and high-precision matching method based on an improved ORB algorithm is proposed for SAR images. The subpixel SAR-OFAST method is used to improve the detection accuracy of keypoints in the proposed method, and the geometric positioning information attached to SAR images is used to reduce the search area among master–slave SAR images. A method of block matching is also employed, which can effectively save computing resources. Experimental results on several pairs of SAR images of identical resolution with

identical observation orientation but diverse incidence angles demonstrate that the proposed method has high efficiency and accuracy in matching images with identical resolutions.

Acknowledgments

This work was supported by the National Key Research and Development Program of China (2020YFA0713501, 2020YFA0713503), the Nature Science Foundation of Hunan Province (2020JJ5537), and the Research Foundation of the Education Department of Hunan Province (19C1769).

References

1 H. Bi, G. Bi, B. Zhang, and W. Hong: Proc. 2019 IEEE 11th Int. Conf. Advanced Infocomm Technology (IEEE, 2019) 228–231.
2 C. Harris and M. Stephens: Proc. 1988 4th Alvey Vision Conf. (1988) 147–151.
3 E. Rosten and T. Drummond: Proc. 2006 9th European Conf. Computer Vision (2006) 430–443.
4 D. Lowe: Int. J. Comput. Vision **60** (2004) 91. https://doi.org/10.1023/B:VISI.0000029664.99615.94
5 H. Bay, T. Tuytelaars, and L. Gool: Proc. 2006 9th European Conf. Computer Vision (2006) 404–417.
6 E. Rublee, V. Rabaud, K. Konolige, and G. Bradski: Proc. 2011 IEEE 13th Int. Conf. Computer Vision (IEEE, 2011) 2564–2571.
7 F. Dellinger, J. Delon, Y. Gousseau, J. Michel, and F. Tupin: IEEE Int. Geosci. Remote Sens. Symp. (2012) 3478–3481. https://doi.org/10.1109/IGARSS.2012.6350671
8 F. Dellinger, J. Delon, Y. Gousseau, J. Michel, and F. Tupin: IEEE Trans. Geosci. Remote Sens. **53** (2015) 453. https://doi.org/10.1109/TGRS.2014.2323552
9 S. Wang, H. You, and K. Fu: IEEE Geosci. Remote Sens. Lett. **9** (2012) 649. https://doi.org/10.1109/LGRS.2011.2177437
10 S. Paul and U. C. Pati: IEEE Geosci. Remote Sens. Lett. **16** (2019) 397. https://doi.org/10.1109/LGRS.2018.2872979
11 J. Li, Q. Hu, and M. Ai: IEEE Trans. Image Process. **29** (2020) 3296. https://doi.org/10.1109/TIP.2019.2959244
12 W. Ma, Y. Wu, Y. Zheng, Z. Wen, and L. Liu: IEEE Geosci. Remote Sens. Lett. **14** (2017) 1680. https://doi.org/10.1109/LGRS.2017.2728604
13 S. Paul and U. Pati: IEEE J. Sel. Top. Appl. Earth Obs. Remote Sens. **12** (2019) 2958. https://doi.org/10.1109/JSTARS.2019.2918211
14 S. Paul and U. Pati: IEEE Geosci. Remote Sens. Lett. **15** (2018) 1387. https://doi.org/10.1109/LGRS.2018.2842921
15 C. Tao and Y. Hu: Photogramm. Eng. Remote Sens. **67** (2001) 1347. https://www.researchgate.net/publication/228902962
16 C. Tao and Y. Hu: Photogramm. Eng. Remote Sens. **68** (2002) 705. https://doi.org/10.1007/s00190-002-0259-4
17 R. Touzi, A. Lopes, and P. Bousquet: IEEE Trans. Geosci. Remote Sens. **26** (1998) 764. https://doi.org/10.1109/36.7708
18 R. Fjortoft, A. Lopes, P. Marthon, and E. Cubero-Castan: IEEE Trans. Geosci. Remote Sens. **36** (1998) 793. https://doi.org/10.1109/36.673672
19 J. Bian, W. Lin, Y. Matsushita, S. Yeung, T. Nguyen, and M. Cheng: IEEE Conf. Computer Vision and Pattern Recognition (2017) 2828–2837.
20 Y. Wu, W. Ma, M. Gong, L. Su, and L. Jiao: IEEE Geosci. Remote Sens. **12** (2015) 43. https://doi.org/10.1109/LGRS.2014.2325970